The Planetary Entry Systems Synthesis Tool: A Conceptual Design and Analysis Tool for EDL Systems

Richard E. Otero and Robert D. Braun
Daniel Guggenheim School of Aerospace Engineering
Georgia Institute of Technology
Atlanta, GA 30332-0150
richard.e.otero@gatech.edu

Abstract—Conceptual design of entry, descent, and landing (EDL) systems requires models over several disciplines as well as knowledge regarding the interactions between these disciplines. To ease the conceptual development of an EDL mission segment and to explore the mission design space, the Planetary Entry Systems Synthesis Tool (PESST) was created. The PESST framework estimates the performance and mass of an entry system using user-defined geometry, aerodynamics, flight mechanics, terminal descent guidance, thermal response and mass estimation models. Trade studies can be performed by parameter sweeps to gain an understanding of the design space for conceptual studies.

Several standard atmospheres are available, and either a user-defined or GRAM atmospheric model may be used. In its present form, PESST may be applied to entry studies for Earth, Mars and Venus missions. This framework is broadly applicable to the conceptual study of EDL systems.

A detailed presentation of the PESST tool and each discipline model is provided along with comparisons to historical entry missions for Earth, Mars and Venus. The PESST framework for system level sizing and synthesis allows for the impact of technologies such as inflatable aerodynamic decelerators and guided terminal descent propulsion to be examined at the mission design level. Closing conceptual designs about these major discipline analyses models the effects of design changes on entry mass, peak deceleration, propellant mass, payload mass, and other mission level design constraints.

TABLE OF CONTENTS

[1] 978-1-4244-3888-4/10/$25.00 ©2010 IEEE.
[2] IEEEAC Paper #1331, Version 4.3, Updated 1/3/2010.

1. INTRODUCTION

The Planetary Entry Systems Synthesis Tool (PESST) is a rapid conceptual design tool for entry, descent, and landing systems. This framework has the capability to estimate the performance of an entry system using user-defined geometry, hypersonic aerodynamics, flight mechanics, thermal response, and mass estimation. Earth, Mars, and Venus atmospheric models are preloaded with the additional ability to use either a user-defined or global reference atmosphere model (GRAM).[9] Trade studies can be performed by parameter sweeps to gain an understanding of the design space for conceptual studies. This framework is broadly applicable to conceptual studies of EDL systems.

Figure 1 displays the interactions that the user can have with the framework. Users that desire a graphical interface can use a Java interface that writes input files for the PESST computational core. This core executable can be run either through the graphical interface or from the command line; allowing the scripting of PESST into a larger conceptual design and optimization process. The executable core has been written with Fortran 95, utilizing object-oriented programming to promote code reuse and maintainability. The desired addition of a parametric capability also placed a high priority on the rapid completion of cases. This supported complementing the strength of Java in interface design with the computational speed and libraries available for Fortran 95.

2. DISCIPLINE MODULES

PESST has seven primary modules: geometry, planetary models, aerodynamics, guidance, trajectory analysis, thermal response, and weights and sizing. Each of these modules is responsible for a separate component of the analysis and interact with one another. The modeled passing of information is shown in Figure 2 and displays the design structure matrix (DSM) for this framework.

System Definition

Atmospheric Models— Atmospheric models in the tool are represented through tables of temperature, pressure and density each as a function of altitude. Three atmospheric profiles are provided by the tool: a Mars atmosphere determined from Viking measurements [24], the 1976 U.S. Standard At-

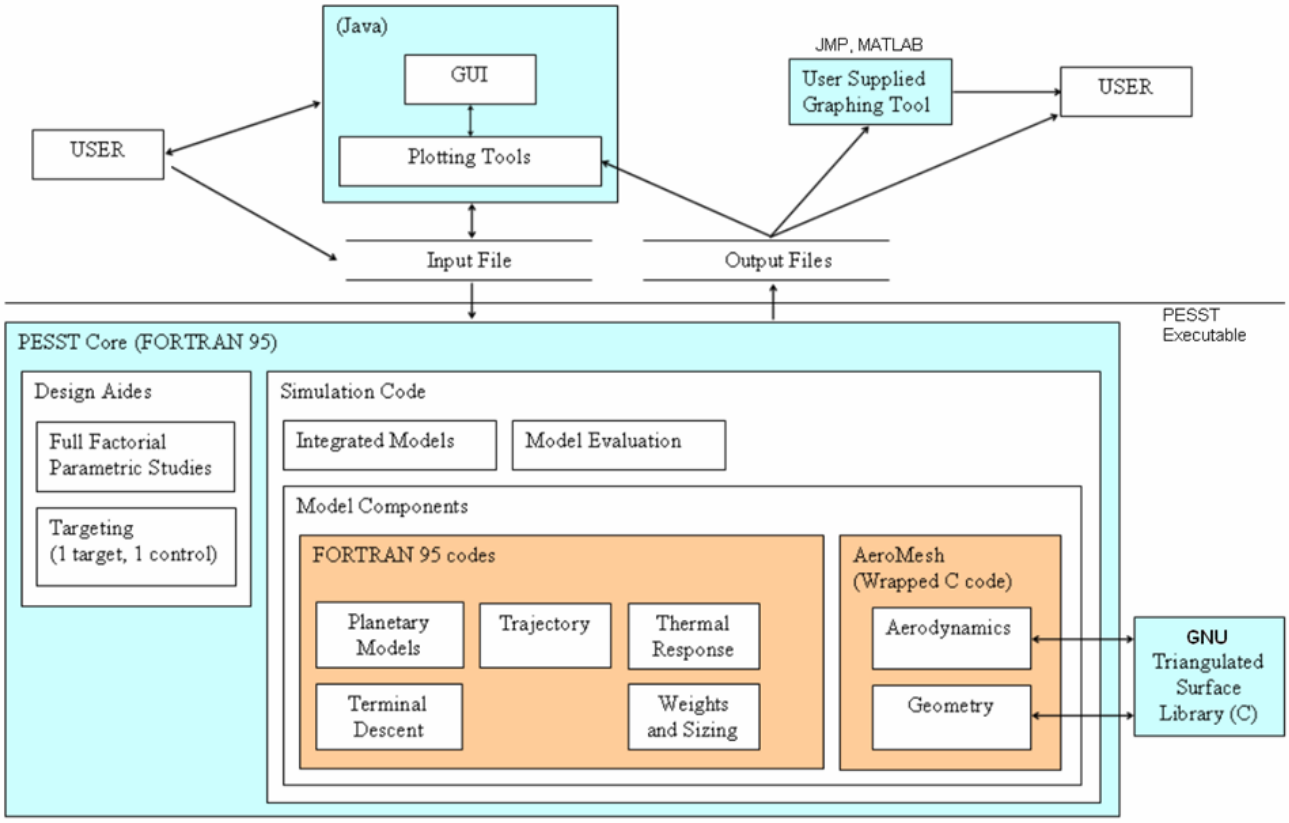

Figure 1. PESST interaction diagram.

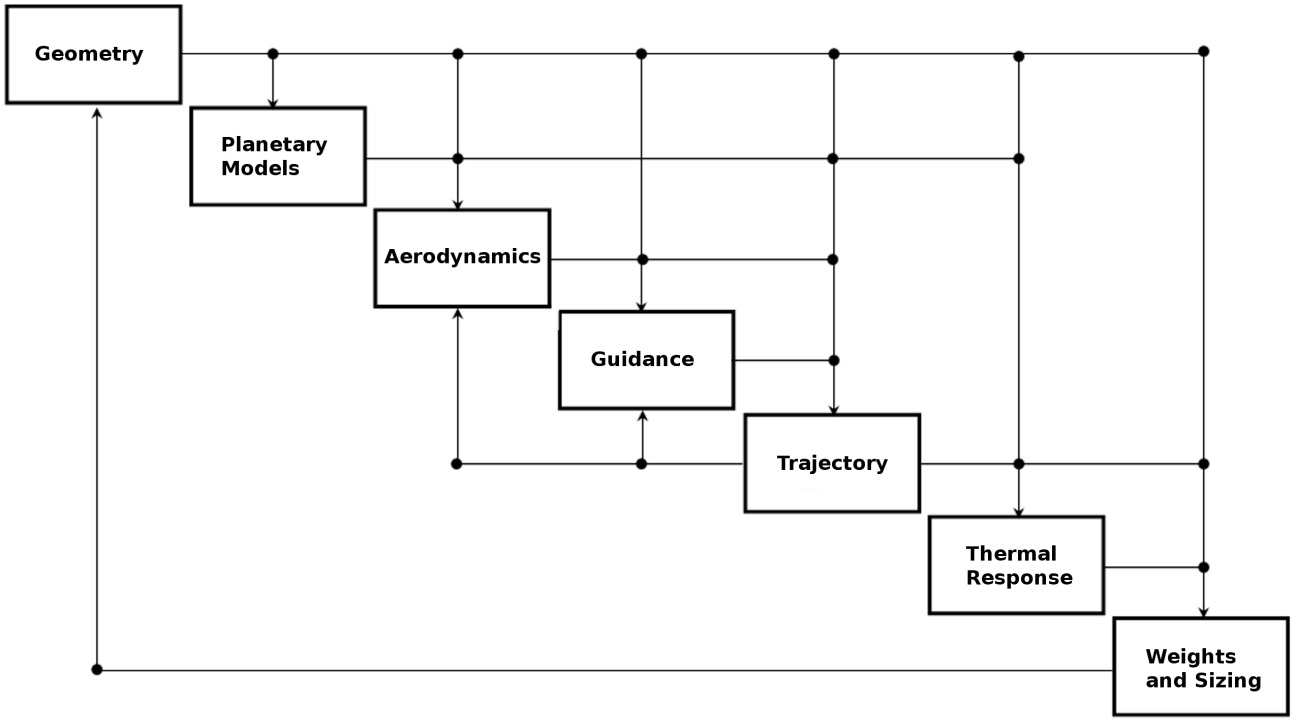

Figure 2. The Design Structure Matrix for PESST.

mosphere for Earth [17], and an averaged model for Venus from Pioneer-Venus data and several of the Russian Venera missons [18]. The reader is referred to these references for the assumptions applied by these models.

PESST has the capability of running a GRAM model and will generate an atmospheric profile for a user-provided latitude, longitude, and entry date. The tool will then use this profile for the trajectory sequence through the atmosphere. The user can also manually specify and modify the atmospheric files used.

Geometry—Analytical expressions exist for the hypersonic aerodynamics of capsules, sphere-cones and biconic shapes. These expressions are very fast but regions of the vehicle that are shadowed from the flow can be a challenge to characterize analytically. The reader is referred to Regan and Anandakrishnan [22] for expressions on geometries with an unshadowed forebody. The work of Grant and Braun [7] is a reference for analytic expressions that characterize vehicles with a shadowed area in the forebody region.

The PESST aerodynamics module is designed to utilize a panel-based method to determine the hypersonic aerodynamics of a shape. An analytical method is simple to implement if the shadowed leeward region can be easily described. A benefit to paneling the shape is the ease in determining the shadowed leeward region of the geometry. A panel is considered shadowed when there is not an acute angle between the normal vector for the panel and the freestream velocity vector, V_∞.

The authors chose to utilize an unstructured triangular meshing algorithm to panel the surface of all shapes examined by the framework. The panel-based mesh allows for one general aerodynamic treatment for both standard and complex entry bodies. Geometrical meshing and aerodynamic calculation takes less than 5 percent of the execution time involved in a run which is normally dominated by the time to size the thermal protection system (TPS).

The mesh of panels for both the standard and arbitrary bodies are generated by the Open Sourced GNU Triangulated Surface (GTS) Library. This LGPL Library can generate a mesh from a descriptive equation or accept an input geometry file. A user can describe their entry body geometry using a CAD package and save the drawing in the common stereolithography (STL) format. The STL format contains a description of the body surface in trianglar panels and is available in most CAD programs. A script from the GTS library converts the STL format to the GTS format of triangular panels used by the library. The PESST aerodynamics module utilizes the grid generated by the GTS library to calculate hypersonic aerodynamics for the described geometry.

The geometry module enables the aerodynamic method by paneling a shape into a large number of flat plates. The shape

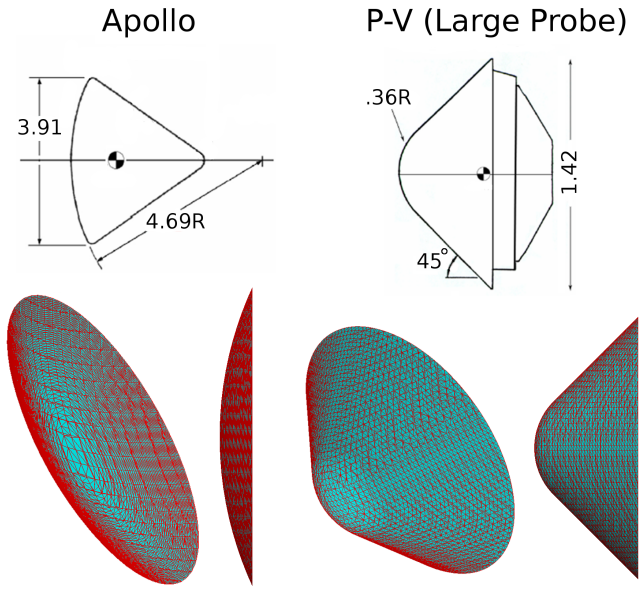

Figure 3. Meshed Geometry for Example Entry Missions.

of the paneled surface is described by providing a 3-D field equation to the GTS Library. For example, the equation for a sphere, $x^2 + y^2 + z^2 - r = C$, describes a 3-D surface within this field. The shape equations within PESST specify surfaces where the constant $C = 0$.

Equations of this nature were created for capsules, sphere-cones, and biconic shapes. The user input of forebody information provides the needed inputs for these equations to properly specify the shape of their surfaces (see Figure 3 which shows the required boxed information to generate the displayed meshes). The GTS Library samples from the space, places points where it finds that the field equation is equal to zero, and connects the generated points to form a triangular mesh over the discovered surface of the body. This makes the addition of a new standard entry shape a simple matter of formulating the proper equation to describe the surface shape. The point discovery and mesh generation is handled by the specialized library.

Aerodynamics

PESST enables the use of either classical or modified Newtonian aerodynamics to characterize the vehicle's aerodynamic coefficients. For Newtonian theory, all of the momentum from a fluid particle pointed normal to the surface of a plate is transferred to the plate while any momentum tangential to the plate is left unchanged. Inappropriate for the subsonic flows that Newton originally designed it for, the theory has been found to serve as an excellent approximation for hypersonic flow.[1] The hypersonic behavior of a flat plate is well understood by the use of this theory. By paneling a vehicle's surface, treating each panel individually, and adding the accumulated forces together; the hypersonic aerodynamics for arbitrary shapes can be approximated.

The aerodynamic pressure coefficient along the shadowed side of an entry vehicle is assumed to be zero. This means that only panels that are facing the flow should be evaluated. The triangles formed from the geometric meshing module are each treated as an individual panel for the Newtonian aerodynamic approximation.

Hypersonic Aerodynamics—The pressure coefficient acting on an individual panel is shown in Equation 1 where θ is the angle of the panel surface to the oncoming flow. $C_{p_{max}}$ is set to 2 for classical Newtonian flow which is typically better for slender bodies while a modification from Lees refined the model to better approximate blunt body hypersonic aerodynamics.[15]

$$C_{p_{panel}} = C_{p_{max}} \sin^2 \theta \tag{1}$$

At high Mach numbers, the modified Newtonian approximation for $C_{p_{max}}$ can be found by using the ratio of specific heats (γ) behind the hypersonic shock. The ratio of specific heats cannot be assumed as constant across the shock; especially when assuming the strong shocks typically seen during an entry.[15]

$$C_{p_{max}} = 2 - \epsilon \approx \underbrace{2 - \frac{\gamma_2 - 1}{\gamma_2 + 1} = \frac{\gamma_2 + 3}{\gamma_2 + 1}}_{\text{for large Mach numbers}} \tag{2}$$

The PESST framework estimates this value initially by assuming the classical Newtonian value for maximum C_p ($C_{p_{max}} = 2$) to calculate the aerodynamics. If modified Newtonian aerodynamics is selected, a run of the trajectory module calculates the density increase behind the shock during the hypersonic portion of the entry. An average for ($\epsilon = \rho_1/\rho 2$) is used to update the maximum possible C_p ($C_{p_{max}}$) and the aerodynamics is refined to a tolerance.

The maximum C_p has a slight Mach dependence that is discounted. C_p becomes essentially independent of Mach at hypersonic speeds, Figure 5 shows the growing insensitivity of drag coefficient to Mach through the supersonic regime. Drag coefficient is a function of pressure coefficient so the diagram also demonstrates the insensitivity of C_p at larger Mach numbers.

After evaluating the pressure coefficient for the triangular plate, the components of the force acting in the x and z directions are found to place the force into the body frame of the entry vehicle, refer to Figure 4. The normal vector for the plate $\bar{n}$ is used to determine the component of C_p that should be applied to each component direction in the body frame. The contribution for each windward panel in the shape is then summed to obtain the contribution over the entire body, Equations 3 and 4.

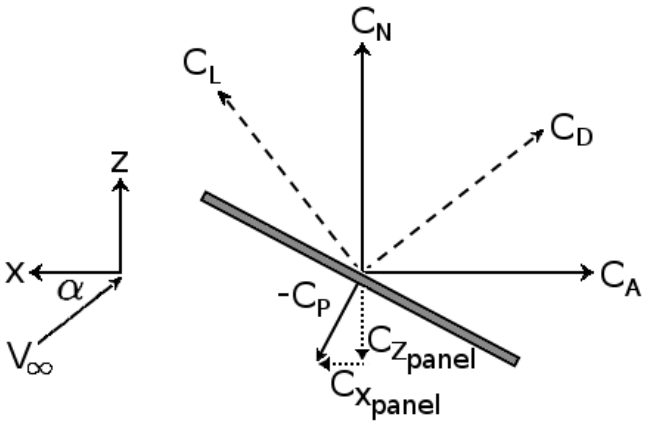

Figure 4. Reference frame for aerodynamic calculations.

$$C_{X_{total}} = \sum_{\text{windward panels}} -C_{p_{panel}} A_{panel} \frac{n_x}{\mid \bar{n} \mid} \tag{3}$$

$$C_{Z_{total}} = \sum_{\text{windward panels}} -C_{p_{panel}} A_{panel} \frac{n_z}{\mid \bar{n} \mid} \tag{4}$$

The forces in the body frame are divided by the reference area to find for C_A which is axial to the body and C_N which is the coefficient normal to the body axis, Equations 5 and 6.

$$C_A = \frac{-C_{X_{total}}}{A_{ref}} \tag{5}$$

$$C_N = \frac{C_{Z_{total}}}{A_{ref}} \tag{6}$$

Forces are now translated from the body frame to the aerodynamic frame of the vehicle where the drag vector is parallel to the incoming velocity vector, assuming the body to be stationary with respect to the reference frame in Figure 4. The flight path angle α is used for the rotation between the body and aerodynamic frames, Equations 7 and 8.

$$C_L = C_N \cos \alpha - C_A \sin \alpha \tag{7}$$

$$C_D = C_N \sin \alpha + C_A \cos \alpha \tag{8}$$

Users are also able to specify their own aerodynamics for this module. For example, the deployment of inflatable aerodynamic decelerators or parachutes are specified by aerodynamic files that become actively used during the duration of their deployed use (see Figure 5 for the aerodynamic values). The calculated aerodynamics for the vehicle are temporarily

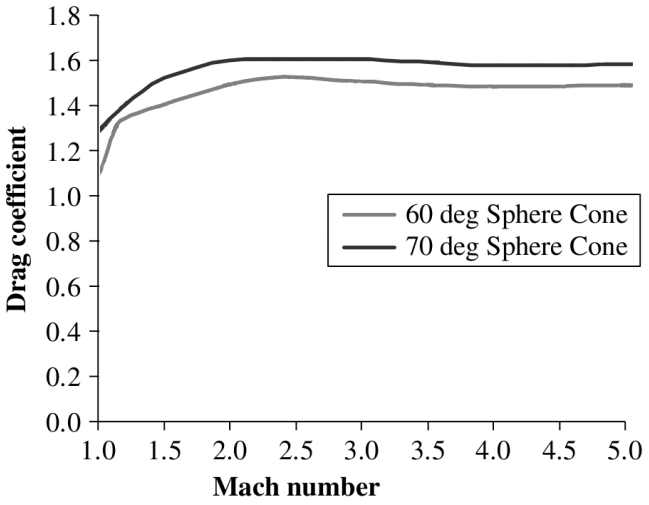

Figure 5. Coefficient of drag information for sphere-cone, IAD and DGB parachute.[3]

replaced by the aerodynamics from the specified files. Using the same mechanism, the users can define their own aerodynamics to override the computed aerodynamics during a trajectory evaluation.

Flight Mechanics

Several books and references have used planet-relative kinematic equations for hypersonic entry bodies that describe the time derivatives of longitude, latitude, radial distance, azimuth, flight path angle, and velocity.[11], [22] When using the prior approach, to determine the derivatives for azimuth and the flight path angle, the equations were divided by the current velocity (i.e., $\dot{\theta} \sim \frac{1}{V}$ and $\dot{\psi} \sim \frac{1}{V}$). During terminal descent, when the velocity became small, the trajectory equations became poorly behaved and were not valid for determining the thrust vector to command. PESST has moved away from this approach after incorporating terminal descent guidance algorithms into the framework.

In the present implementation, the equations of motion are switched to a planet-centered inertial reference frame, this will be referred to as the inertial frame. When converting to/from this reference frame the transformation matrix is considered as being solely a function of the planet's rotation about a stationary z-axis, during the entry. The vector formulation for the equations of motion in the inertial frame is both well behaved, over a full range of velocities, and it does not experience the equation singularities that can appear with certain angles in planet-relative equations.

$$\begin{bmatrix} \dot{\mathbf{r}}^{\mathbf{I}} \\ \dot{\mathbf{v}}^{\mathbf{I}} \\ \dot{m} \end{bmatrix} = \begin{bmatrix} \mathbf{v}^{\mathbf{I}} \\ \sum \mathbf{F}^{\mathbf{I}}/\mathbf{m} \\ -|\mathbf{T}|/(g_o\, I_{SP}) \end{bmatrix} \tag{9}$$

PESST now utilizes three degree-of-freedom (DOF), with

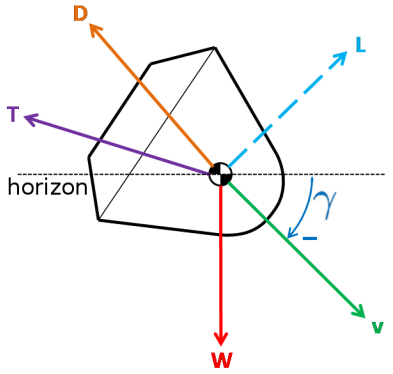

Figure 6. Entry system free-body diagram.

bank angle modulation, equations of motion to determine the time history of the entry system's state, Equation 9. The trajectory is propagated using a variable-step 4th-order Runge-Kutta integrator with 5th-order error truncation over a fixed time-span from a set of planet relative initial conditions (altitude, velocity, flight path angle, azimuth angle, latitude, longitude, angle of attack, and bank angle) until the end of the simulation. The starting condition is transformed to inertial space and the movement of the vehicle is integrated inertially.

As the PESST framework converts angles to/from inertial coordinates, the framework does not experience angular singularities; it is effectively post processing to get the flight path angle or any other angle.

This treatment allows for forces to be easily added or removed for the entry vehicle; as only the inertial summation of forces on the body is required for each time step through the integration. The forces tracked by the framework, shown in Figure 6, are: drag, lift, the weight vector due to gravity, and a thrusting vector if guidance is active. The method is more maintainable and extendable than the earlier angular derivatives. For example, the addition of wind effects could be enabled through the manipulation of the velocity vector. Alternatively, a buoyancy force, useful for Titan entries, could also be easily appended to the summation of forces.

$$L = -q\, C_L\, A_{ref} \tag{10}$$

The lift magnitude is determined from Equation 10. The reference area of the vehicle is A_{ref} and q is the dynamic pressure. The direction of the lift vector is perpendicular to the velocity vector and is rotated by the bank angle specified for the vehicle.

$$\mathbf{D} = -q\, C_D\, A_{ref} \frac{\mathbf{v}^{rel}}{|\mathbf{v}^{rel}|} \tag{11}$$

The vector for vehicle drag is parallel to the planet relative velocity vector and is specified by Equation 11.

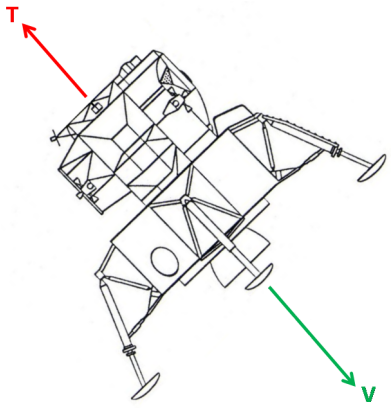

Figure 7. Gravity turn thrust orientation. Lander image from [20].

$$\dot{m} = \frac{-|\mathbf{T}|}{g_o \, I_{SP}} \tag{12}$$

The rocket equation is used to estimate the mass loss during propulsive maneuvers. Discrete mass drop events, such as the drop of a heat shield, are modeled by a discontinuous drop to the system mass at the drop point.

Terminal Descent Guidance Algorithms

Gravity Turn—PESST allows for the specification of a constant thrust gravity turn event. In a gravity turn, the thrust vector is in the opposing direction from the current velocity vector, Figure 7. This causes the vehicle to be turned towards a vertical descent by the gravitational force on the vehicle. This method targets for a specified velocity at a given altitude and a constant thrust gravity turn was utilized for the terminal descent of Lunar Surveyor and other missions.

An analytic equation for the thrust magnitude can be obtained if a small nadir angle is assumed. PESST avoids the small nadir angle assumption by numerically determining how well the constant thrust value meets specified targets. This is implemented by specifying an initial fixed thrust magnitude and propagating the equations of motion to determine how well that thrust value meets the velocity and altitude targets. Newton iteration is used to converge towards the fixed thrust magnitude needed for the desired final altitude and velocity magnitude. Specifying the maximum thrust magnitude for the engine would show the latest possible ignition time that would successful match the velocity and altitude targets.

Analytical Control Law—The work of D'Souza [6] developed an analytic control law that assumes a planar non-rotating planet with no atmosphere. This was found to be suitable for Mars applications that required a first-order model for pinpoint landing. This analytic method is an unconstrained energy-optimal propulsive terminal descent algorithm that meets the necessary and sufficient conditions for an optimal control law.[25]

$$J = \Gamma \, t_f + \frac{1}{2} \int_{t_o}^{t_f} \mathbf{a}^T \mathbf{a} \, dt \tag{13}$$

The D'Souza algorithm seeks to minimize the performance index shown in Equation 13. For the current PESST implementation, the weighting on the final time Γ has been set to zero. It has been shown that the control law which minimizes this performance index is given by Equation 14, given the vector definitions from the vector Equations in 15.[6]

$$\mathbf{a} = -4\frac{\mathbf{\Delta v}}{t_{go}} - 6\frac{\mathbf{\Delta r}}{t_{go}^2} - \mathbf{g} \tag{14}$$

$$\mathbf{\Delta r} = \begin{bmatrix} r_1 - r_{1_f} \\ r_2 - r_{2_f} \\ r_3 - r_{3_f} \end{bmatrix} \quad \mathbf{\Delta v} = \begin{bmatrix} v_1 - v_{1_f} \\ v_2 - v_{2_f} \\ v_3 - v_{3_f} \end{bmatrix} \quad \mathbf{g} = \begin{bmatrix} 0 \\ 0 \\ g \end{bmatrix} \tag{15}$$

The time-to-go, t_{go}, is provided as the real positive root to equation 16. This equation is solved by Newton iteration which provides rapid convergence while mitigating the numerical issues that can be associated with analytical root equations.[25]

$$t_{go}^4 - 2\frac{\mathbf{\Delta v^T \Delta v}}{\Gamma + \frac{g^2}{2}} t_{go}^2 - 12\frac{\mathbf{\Delta v^T \Delta r}}{\Gamma + \frac{g^2}{2}} t_{go} - 18\frac{\mathbf{\Delta r^T \Delta r}}{\Gamma + \frac{g^2}{2}} = 0 \tag{16}$$

The thrust that is commanded by the guidance algorithm at each point in time is given by Equation 17. When the guidance event is active, the thrust is computed in a closed loop sense at each timestep through the equations of motion. The reader is referred to the work of Steinfeldt, et al. for performance and accuracy comparisons with this analytic control law.[25]

$$\mathbf{T} = m\left(-4\frac{\mathbf{\Delta v}}{t_{go}} - 6\frac{\mathbf{\Delta r}}{t_{go}^2} - \mathbf{g}\right) \tag{17}$$

Thermal Response

Modeling of a thermal protection system requires the modeling of an energy balance that involves some subset of the processes that occur during the ablation of the material. Figure 8 shows some of the energy and mass-related processes that are involved during an ablative entry. In the PESST thermal modeling, convective and radiative fluxes will be explicitly modeled, while surface recession will be indirectly modeled by the use of an experimental correlation called the heat of ablation.

The problem of estimating the TPS thickness required for an entry is decomposed into two sub-problems; the thickness that will be ablated during the descent and the thickness required to insulate the vehicle. The two thicknesses are added together to estimate the composite thickness required by the TPS material to survive ablation in the heating environment and adequate insulation for the vehicle.

Heating Environment—The Sutton-Graves heating relationships are used to estimate the degree of convective stagnation point heating.[26] The form of this relationship is shown in Equation 18 where $\mathbf{v}^p$ is the planet relative velocity and r_n is the effective nose radius of the vehicle. The Sutton-Graves convective constant k is a function of the composition of the atmosphere. The convective relation was designed for an arbitrary atmosphere.[26] PESST currently uses pre-computed values for Earth, Mars and Venus but future work could dynamically calculate the convective constant from the user's specification of the atmospheric composition.

$$\dot{q}_{conv} = k\frac{\sqrt{\rho}\,|\mathbf{v}^p|^3}{\sqrt{r_n}} \tag{18}$$

A general radiative relation for an arbitrary atmosphere is an open problem. Radiative relations for Earth and Mars are supplied by the work of Tauber and Sutton, the form of the relation is shown in Equation 19.[27] The constants C, a, b, and a function of the planet relative velocity v are defined for Earth or Mars. A pre-publication radiative expression for Venus was provided to the authors by Dr. Tauber. The data used to generate the Venus relation can be found from the work of Page and Woodward.[19]

$$\dot{q}_{rad} = C\, r_n^a\, \rho^b\, f(|\mathbf{v}^p|) \tag{19}$$

The total heating is considered as the summation of the radiative and convective heating, Equation 20.

$$\dot{q}_{tot} = \dot{q}_{conv} + \dot{q}_{rad} \tag{20}$$

Thickness Ablated—The heating from the surface into the material is required to size the insulation thickness required from the TPS material. Equation 21 is an energy balance where the left hand side of the equation represents energy (heat) traveling into the material and the right hand side represents the other processes occuring at the ablating surface.

$$-k\frac{\partial T}{\partial x} = -\dot{q}_{cw}\frac{H_r - H_{air}^{T_w}}{H_r} + \tag{21}$$

$$\sigma\,\varepsilon\,T_w^4 + \tag{22}$$

$$\rho\,\dot{s}\,\Delta H_v + \tag{23}$$

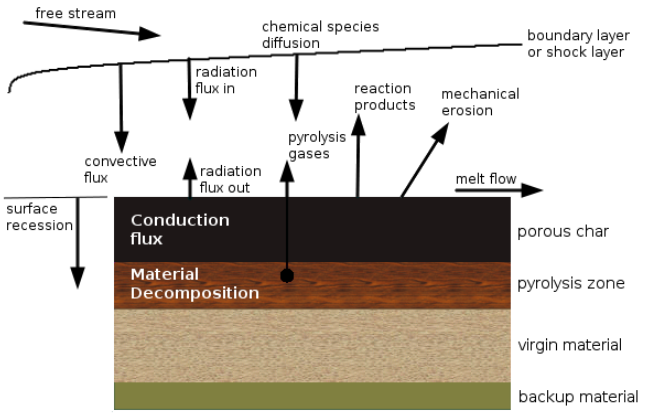

Figure 8. Processes during the ablation of a material [14].

$$\rho\,\dot{s}\,\eta\,\left(H_r - H_{air}^{T_w}\right) \tag{24}$$

The right side of Equation 21 shows the convective net heat flux into the surface without ablation.[5] The term from Equation 22 shows the heat flux re-radiated from the surface of the heat shield. The term from Equation 23 calculates the amount of energy absorbed through the vaporization of the ablating material. The last term, Equation 24, shows the amount of heat absorbed through the transpiration of ablation gases into the flow.[5]

$$\left(k\frac{\partial T}{\partial x}\right)_{ss} = \rho\dot{s}\,C_p\,(T_w - T_o) \tag{25}$$

Assuming steady state ablation, the equation for the heat traveling into the material simplifies to Equation 25. Substituting Equation 25 into Equation 21 forms Equation 26.

$$\dot{q}_{cw}\left(\frac{H_r - H_{air}^{T_w}}{H_r}\right) - \sigma\varepsilon T_w^4 = \rho\dot{s}\,\left(C_p\Delta T + \Delta H_v + \eta\Delta H\right) \tag{26}$$

Manipulating the terms for the equation forms the definition for the experimental relation Q^*, the heat of ablation. The central terms of Equation 27 are composed of values that can be tested in a laboratory setting. It is through experimental testing that a curve for Q^* is found.

$$Q^* = \frac{\dot{q}_{cw}\left(\frac{H_r - H_{air}^{T_w}}{H_r}\right) - \sigma\varepsilon T_w^4}{\rho\dot{s}} = \left(C_p\Delta T + \Delta H_v + \eta\Delta H\right) \tag{27}$$

As a simple ablation relationship is desired, an approximation is made to the experimental curve found for the heat of

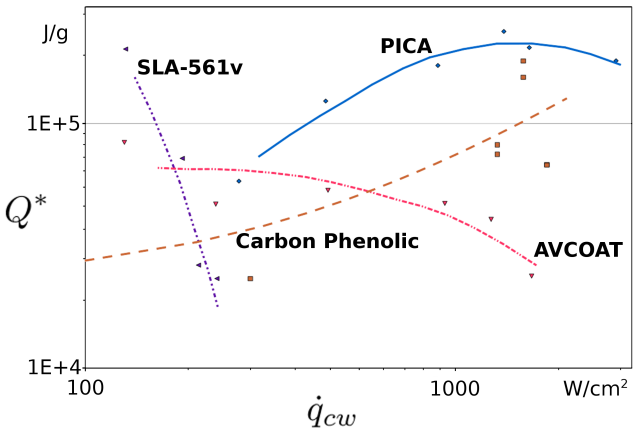

Figure 9. Heat of ablation vs. cold wall heat rate. [21], [29]

ablation. The rate of thickness lost due to steady state ablation $\dot{s}$ is less than the value shown in Equation 28. $\dot{q}_{cw}$ is the rate of cold wall heating at the surface; this is taken as equal to the total rate of heating computed in Equation 20. Given a curve for Q^* vs. $\dot{q}_{cw}$ a conservative estimate can be made for the rate of thickness lost due to steady state ablation. This calculation would be integrated throughout the trajectory to calculate the total thickness lost due to ablation.

$$\dot{s} < \frac{\dot{q}_{cw}}{\rho\, Q^*} \tag{28}$$

An example experimental curve for Q^* vs. $\dot{q}_{cw}$ is shown in Figure 9.

Thickness used for Insulation—The computed temperature at the surface of the heat shield serves as a boundary condition to calculate the transient in-depth temperature behavior through the material. This is used to calculate the thickness of the material required to insulate the structure behind the TPS system to a specified boundary temperature limit. The 1-D heat conduction equation where density, specific heat C_p and the thermal conductivity k vary with position is given by Equation 29.

$$\frac{\partial}{\partial x}\left(k\frac{\partial T}{\partial x}\right) = \rho C_p \frac{\partial T}{\partial t} \tag{29}$$

This in depth equation can be solved by either an explicit or implicit method. Here an implicit method has been used to track the response of the material to the application of surface heating. The Crank-Nicolson implicit method used is unconditionally stable and the finite difference approximation has a truncation error of order $O[(\Delta t)^2, (\Delta x)^2]$.

$$\frac{\partial \rho}{\partial t} = f\left(\rho, T\right) \tag{30}$$

Table 1. TPS Material Density.

TPS Material	**Density** ($\mathrm{kg/m^3}$)
PICA	227.4
SLA-561v	264.3
FM5055	1435.4

The decomposition rate is modeled by a three component Arrhenius relation shown by Equation 31. The constants required to use the equation for PICA and Carbon Phenolic are provided in the attached Appendix.

$$\left.\frac{\partial \rho}{\partial t}\right)_x = -B \exp\left(\frac{-E}{RT}\right) \rho_o \left(\frac{\rho - \rho_r}{\rho_o}\right) \tag{31}$$

To compute the density for the composite material, the densities for each component need to be included, Equation 32.

$$\rho = \Gamma\left(\rho_{A_{\text{resin}}} + \rho_{B_{\text{resin}}}\right) + (1-\Gamma)\,\rho_{C_{\text{fiber}}} \tag{32}$$

Refer to the tables in the Appendix for thermal material information used the PESST framework to perform these calculations.

Mass Estimation

Thermal Protection System Sizing—The ablation rate $\dot{s}$ is integrated over the trajectory to estimate the thickness lost from ablation. The stagnation heat conducted into the material is used to size the minimum thickness required to keep the interior wall of the material below a user specified bondline temperature. Both processes are considered as decoupled so the thicknesses are added to give a final uniform heatshield thickness.

The heatshield mass is computed from the provided area covered by the heatshield A, the density of the heatshield ρ_{tps} (Shown in Table 1), and the computed thickness.

$$m_{struct_{tps}} = 0.08\, m_{entry} \tag{33}$$

The structural mass of the heatshield is estimated by the mass estimating equation 33. The structural mass is added to form the final estimate for a constant thickness heatshield, see Equation 34

$$m_{heatshield} = m_{struct} + A\, t_{tps}\, \rho_{tps} \tag{34}$$

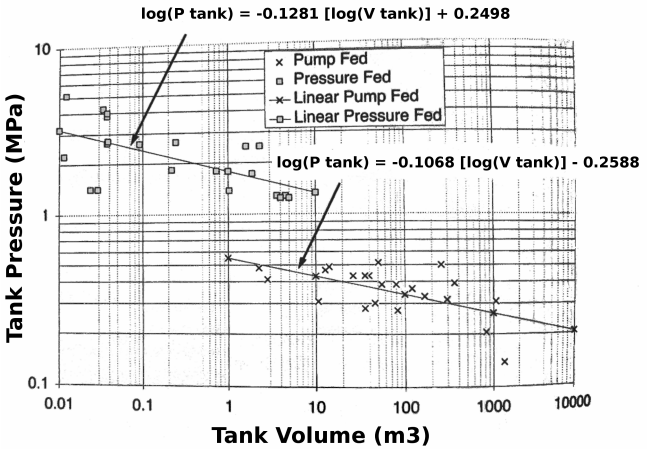

Figure 10. Tank Pressure Fits by Engine Type.[8]

Table 2. Tank Mass Factors.

Tank Material	**Tank Mass Factor** (m)
Al	2500
Ti	5000
Ti with Carbon Fiber	10000

Propulsion System Sizing—Any thrust events performed during the trajectory add to the budgeted fuel requirement by integrating the $\dot{m}$ computed through the rocket equation, see Equation 12. The density for the fuel and oxidizer and O-F ratio are used to determine the volume requirements for each liquid.

The operating pressure for the tank is determined from the engine type and tank volume using the data regression in Figure 10 to historical data of different engine types. This operating pressure is used to size the volume of Helium required to act as a pressurant for this tank, in pressure-fed systems. The reader is referred to [8] for further details.

The pV/W method is utilized to calculate the tank mass without specified tank dimensions. This method requires the specification of a tank mass factor ϕ_{tank} that describes the strength of the tank material. A completely metallic tank has a tank factor equal to 2500 m, with reinforcing materials, the tank factor can rise to 10000 m.[8] The values used by PESST for the three available tank materials are shown in Table 2.

$$m_{tank} = \frac{f_{safety}\, P_{tank}\, V_{tot}}{g_0\, \phi_{tank}} \tag{35}$$

The pV/W method uses the burst pressure for the tank $P_{burst} = f_{safety}\, P_{tank}$ (Pa), tank volume V_{tot} (m^3), and tank factor ϕ_{tank} (m) to calculate for the tank mass in kilograms. The burst pressure for the tank is estimated in PESST as the operating pressure times a safety factor equal to 1.5.

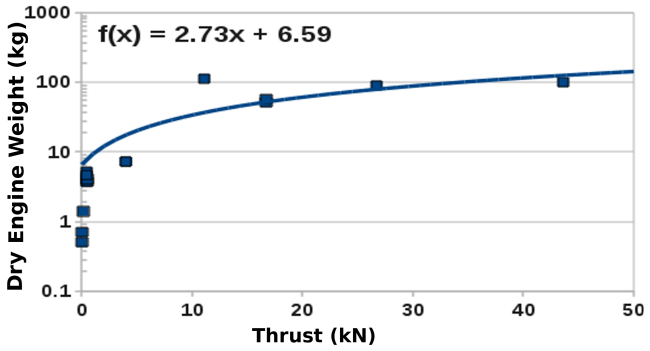

Figure 11. Sizing Fit for Monomethyl Hydrazine Engines. Historical data from [8].

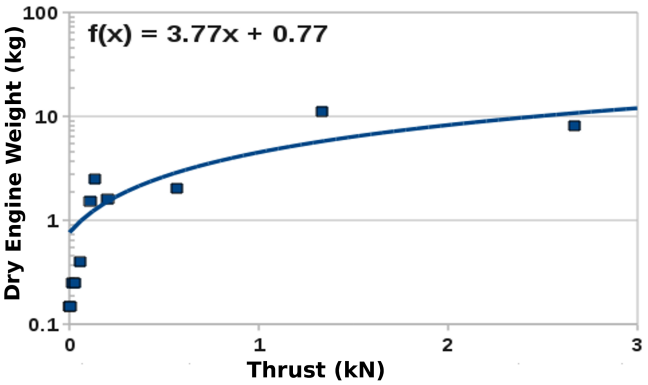

Figure 12. Sizing Fit for Monopropellant Hydrozine Engines. Historical data from [8].

This method is utilized to determine the mass for the fuel, oxidizer, and potential pressurant tanks.

Regressions through historical engine mass data are used to size for the engine based on the engine maximum thrust and fuel type. The equations in Figures 11,12,13 use x in kN to compute the dry weight of the engine in kg on these semi-log charts.

The LOX/CH_4 engine weight data provided from [12] cited the engine wet weight. Six percent of the weight cited in the paper was removed to regress the estimated dry weight, Figure 13. The lines and valves for the engine are assumed to weigh as much as the engine itself.

The summation of the masses for the fuel tanks, pressurization system (pressurant + pressurant tank), engine, lines and valves is given for the propulsion system mass.

Parachute System Sizing—

$$\begin{aligned} F_{max} &= C_k\, q_{deploy}\, C_D\, A \\ F_{design} &= f_{safety}\, F_{max} \end{aligned} \tag{36}$$

The parachute sizing module models an infinite mass inflation

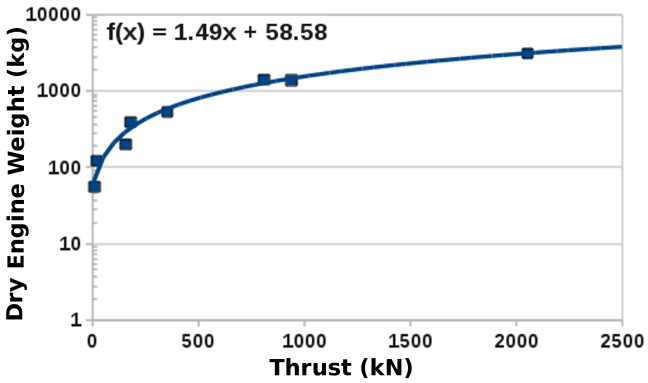

Figure 13. Sizing Fit for LOX/Methane Engines. Prototype results from [12].

with the peak load occurring at full parachute inflation. The parachute is sized based on this peak load with a safety factor equal to 1.5. The C_k method was utilized with a $C_k = 0.6$ for DGB parachutes and the area $A = \pi \left(\frac{D_o}{2}\right)^2$. The material properties for kevlar are used to size for the radials, lines and riser. The tensile strength of Nylon fabric and F_{design}, from Equation 36, is used to determine the thickness required for the parachute fabric. After the parachute is sized, a mortar is sized by $m_{mortar} = 1.48\, m_{para}^{0.5}$ which was derived from historical mortar data.[13]

Backshell and Structural Sizing—

$$m_{backshell} = 6.7582\, m_{entry}^{0.4116} \tag{37}$$

The backshell and primary structural mass is estimated by Equation 37 and assumes that the backshell is integrated with the structure of the vehicle. For smaller vehicles, where the regression would extrapolate, the mass fraction for the backshell and primary structural mass is capped at 25%.

3. Comparisons to Historical Missions

PESST predictions for historical missions are included to display the suitability and flexibility of the framework for conceptual design.

The reconstruction for Mars Pathfinder comes from the work of Christian, et al. [2], adapted by the work of Soumyo Dutta. Their work creating a Pathfinder reconstruction with an extended Kalman filter. Heating information is taken from Milos, et al. [16]. The reconstructed Pathfinder atmosphere is used for both the PESST and POST trajectory. Both PESST and POST specify the same dynamic pressure trigger for parachute inflation and the same aerodynamics for the Disk-Gap Band parachute. Differences in the implementation of the infinite mass parachute inflation model may explain the descrepancy between to two tools. Otherwise, all three show good agreement for the purposes of conceptual design, Table 3.

Table 4. Mass Comparison to Pathfinder.

Element (kg)	**Flight Mass**	**PESST**	**Diff Flight (%)**	**Flight Mass (%)**
Entry Mass	585.3	585.0	-0.1	-
Heatshield	64.4	75.0	16.5	11.0
Backshell and Structure	56.9	93.0	63.4	9.7
Parachute	9.8	17.0	74.4	1.7
Payload	360.0	360.0	0.0	61.5
Remainder	94.2	40.0	-57.6	16.1

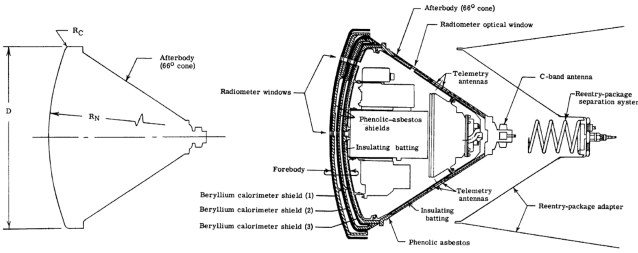

Figure 14. Fire II Multi-Heatshield Structure [4].

The Fire II mission was designed to sample from the entry heating environment as a precursure to the Apollo missions. To accomplish this mission, the vehicle utilized three highly instrumented heatshields. Each segment of the heating environment, Figure 15, was sampled by a fresh heatshield. The instrumented Beryllium layer of each heatshield would melt through to a phenolic asbestos backing. The phenolic separated into four sections, during an ejection event, to expose the next heatshield, Figure 14. The mission has several mass drop events and a change in both aerodynamics and heating behavior after each heatshield deployment making it a good case to showcase the flexiblity of PESST.

The mass drops were modeled from masses and times provided in [23]. After the first heatshield drop, the aerodynamics tool was run again to refresh the aerodynamics and nose radius used by the heating relations. The mission experienced an osculation in angle of attack, about zero, for a large segment of the trajectory so this run approximated the angle of attack as zero. The sideslip and the total angle of attack were not treated by PESST.

PESST shows good agreement with the mission in Table 5. PESST used the U.S. Standard 1976 Atmosphere. A designer with a timeline of events and rough mass estimates could run several cases on this mission to gain a better understanding of the design space being examined.

A conceptual design tool needs to predict the full system with enough accuracy to inform initial design decisions. Martian

Table 3. Trajectory and Heating Comparison to Mars Pathfinder.

Event	Units	Flight Reconstruction [2], [16]	POST	PESST	Diff from POST (%)	Diff from Reconst. (%)
Initial Conditions						
Time from Entry	s	0	0	0	-	-
Altitude	km	128.0	128.0	128.0	-	-
Relative Velocity	m/s	7479.0	7479.0	7479.0	-	-
Flight Path Angle	°	-13.65	-13.65	-13.65	-	-
Peak Heat Rate Conv (Rad)	W/cm^2	118.0 (5.5)	115.5 (-)	115.3 (4.8)	-0.2 (-)	-2.3 (-12.4)
Time from Entry	s	66.0	62.3	62.2	-0.2	-5.8
Altitude	km	42.3	40.4	40.8	0.9	-3.7
Relative Velocity	m/s	6589.6	6512.9	6552.2	0.6	-0.6
Heatload Conv (Rad)	J/cm^2	3800.0 (88.7)	4335.0 (-)	4330.7 (84.2)	-0.1 (-)	14.0 (-5.0)
Peak Deceleration	Earth-g	15.8	16.3	16.3	-0.3	2.7
Time from Entry	s	77.8	72.9	73.4	0.7	-5.6
Altitude	km	33.1	31.8	31.8	-0.1	-4.1
Relative Velocity	m/s	5055.3	5032.9	5029.2	-0.1	-0.5
Parachute Full Inflation	Earth-g	6.0	7.5	6.0	-20.3	0.0
Time from Entry	s	173.2	161.3	163.0	1.1	-5.9
Altitude	km	7.6	8.2	8.2	-0.4	7.4
Relative Velocity	m/s	338.5	369.8	360.6	-2.5	6.5
Heatshield Drop						
Time from Entry	s	192.2	182.6	192.0	5.1	-0.1
Altitude	km	6.9	6.5	5.9	-9.7	-15.0
Relative Velocity	m/s	94.3	82.2	79.0	-3.8	-16.2
Trajectory Termination						
Time from Entry	s	298.0	290.0	285.2	-1.7	-4.3
Altitude	m	130.7	128.6	127.4	-0.9	-2.5
Relative Velocity	m/s	63.3	53.7	56.9	6.0	-10.1

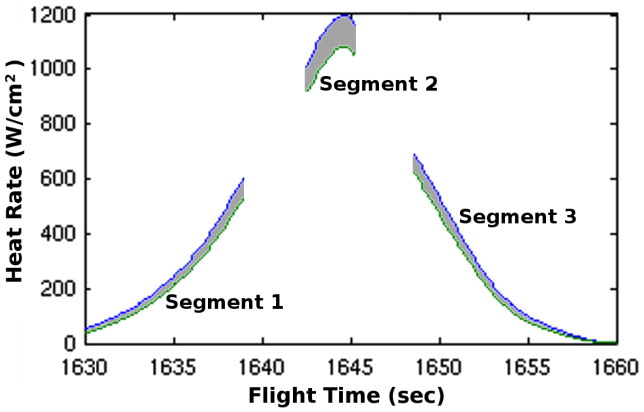

Figure 15. Estimated Range of Uncertainty for Fire II Heat Rate [4].

mission designers can be used to designing probes to withstand 20 g_E but PESST can allow them to better understand a new entry environment, such as Venus, where missions commonly design for 250 g_E. In this way, the framework is broadly applicable to better understanding EDL systems without much effort or time. The two examples above show that complex systems such as Fire II, Table 5, can be modeling quickly to understand the first-order interactions in the design.

4. Application to Pending Sample Return Mission

The Hayabusa mission, if successful, will be the first mission to return samples from an asteroid to Earth. Due to an altitude change while orbiting its asteroid, likely caused by leaked

Table 5. Trajectory and Heating Comparison to Fire-II Mission.

Event	Units	Flight Reconstruction [4], [23]	PESST Geometry A	PESST Geometry B	Diff from Reconst. (%)
Initial Conditions			Start Geo A	Start Geo B	
Time from Entry (Flight Time)	s	0 (1617.7)	0 (1617.7)	24.44 (1642.14)	-
Altitude	km	122.18	122.18	55.73	-
Relative Velocity	m/s	11344.7	11344.7	10721.18	-
Flight Path Angle	°	-14.74	-14.74	-13.31	-
Peak Heat Rate (Conv+Rad)	W/cm^2	1197-1081		1091	In Range
Time from Entry (Flight Time)	s	27 (1644.7)		25.7 (1643.4)	-4.8
Altitude	km	49.11		52.57	7.0
Relative Velocity	m/s	9955.8		10407	4.5
Flight Path Angle	°	-13.24		-13.25	-0.1
Heatload (Conv+Rad)	J/cm^2	13051		12353	-5.3
Peak Deceleration	Earth-g	~ 74		80.2	8.4
Time from Entry (Flight Time)	s	32.5 (1650.2)		32.12 (1649.82)	-1.2
Altitude	km	38.62		39.69	2.8
Relative Velocity	m/s	6836.8		6892.3	0.8
Flight Path Angle	°	-13.12		-13.09	0.2

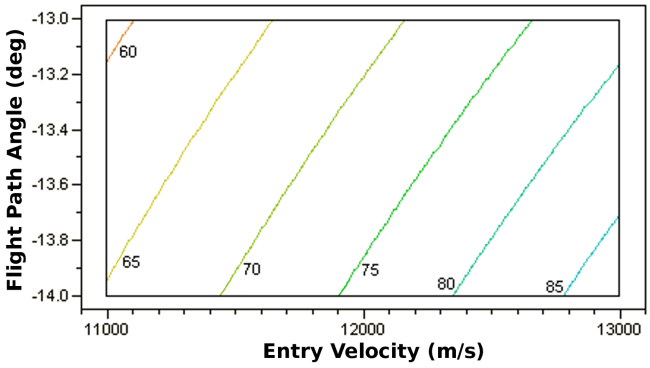

Figure 16. Hayabusa Peak Sensed Deceleration, Earth-g.

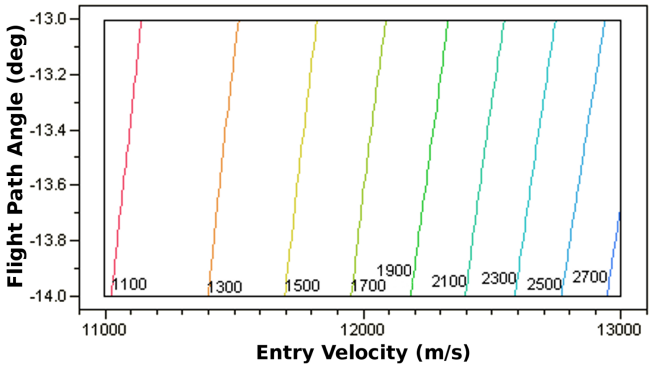

Figure 17. Hayabusa Peak Heat Rate, $W/cm.^2$

fuel, the trip and re-entry at Earth was rescheduled from 2007 to June 2010. PESST has a parametric study capability that allows it to run and organize cases over the space of possible entries. This allows PESST to better expose the trade offs between scenarios. Eight hundred cases were run to cover a span of flight path angle and entry velocity for Hayabusa's entry, Figures 16, 17, 18.[30]

With a set of initial conditions, these figures show how a designer can gain an understanding of the potential heating environments, heatshield thickness required, peak sensed deceleration and more. The parametric study capability allows the user to automatically assemble the vehicle state at the max, min, or specified value for any output variable; for every case run during a parametric study. The user can run 8000 cases and select that only the output line containing the maximum deceleration will be consolidated into one output file with 8000 lines of data, one line for each case. Automatically grouping lines from output files where a certain output variable is greater-than, less-than or equal-to a value is also available to a user.

5. Conclusions

Conceptual design decisions are better informed by the early application of physics-based tools to the design process. First order tools are often fast enough to be used during parametric studies while still providing information on many of the main

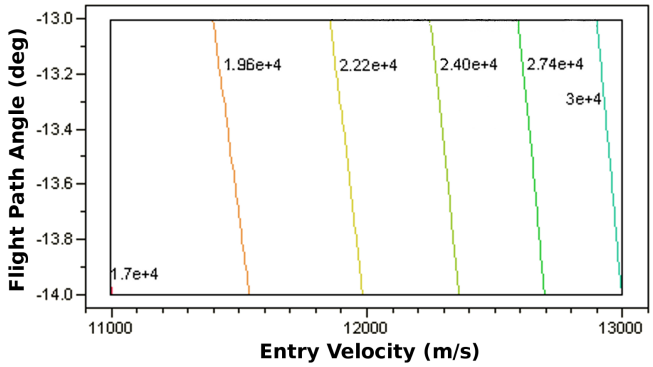

Figure 18. Hayabusa Heat Load, $\mathrm{J/cm}^2$

effects and trades that can now be examined, far earlier in the design process, for entry missions. A detailed examination was made into the methods used to implement each of the entry discipline modules, allowing for the widespread use and critique of these models for entry systems. Several useful tables of public domain information have been converted to SI and appended to this document for the ease of the reader.

ACKNOWLEDGMENTS

The authors would like to thank the Jet Propulsion Laboratory and the Charles Stark Draper Laboratory for their sponsorship of the new PESST framework. The work of Michael J. Grant and Bradley A. Steinfeldt of the SSDL was invaluable towards the incorporation of guidance algorithms into the current framework. The authors remain greatly appreciative of the time provided by Mike Tauber for conversations on radiative heating. Finally, the authors also wish to thank Patrick J. Smith for his work in implementing a very flexible parametric study capability.

REFERENCES

[1] J. D. Anderson. *Hypersonic and High Temperature Gas Dynamics*. AIAA, August 2000.

[2] J. A. Christian, A. M. Verges, and R. D. Braun. Statistical reconstruction of mars entry, descent, and landing trajectories and atmospheric profiles. In *AIAA SPACE 2007 Conference & Exposition*, Long Beach, CA, 18-20 September 2007. AIAA 2007-6192.

[3] I. G. Clark, A. L. Hutchings, C. L. Tanner, and R. D. Braun. Supersonic inflatable aerodynamic decelerators for use on future robotic missions to mars. *Journal of Spacecraft and Rockets*, 46(2):340–352, March-April 2009.

[4] E. S. Cornette. Forebody temperatures and calorimeter heating rates measured during project fire ii reentry at 11.35 kilometers per second. Technical report, Langley Research Center, November 1966. NASA TM X-1305, Unclassified.

[5] J. A. Dec and R. D. Braun. Ablative thermal response analysis using the finite element method. In *47th AIAA Aerospace Sciences Meeting Including The New Horizons Forum and Aerospace Exposition*, January 2009. AIAA 2009-259.

[6] C. D'Souza. An optimal guidance law for planetary landing. In *AIAA*, 1997. AIAA 97-3709.

[7] M. J. Grant and R. D. Braun. Analytic hypersonic aerodynamics for conceptual design of entry vehicles. In *48th AIAA Aerospace Sciences Meeting Including the New Horizons Forum and Aerospace Exposition*, 2010.

[8] R. W. Humble, G. N. Henry, and W. J. Larson. *Space Propulsion Analysis and Design*. McGraw-Hill, 1995.

[9] H. L. Justh, C. G. Justus, and V. W. Keller. Global reference atmospheric models, including thermospheres, for mars, venus and earth. In *AIAA / AAS Astrodynamics Specialist Conference and Exhibit*, Keystone, Colorado, August 2006. AIAA 2006-6394.

[10] M. Keyhani. Verification of thermal analysis codes for modeling solid rocket nozzles. NASA Contractor Report NASA-CR-195248, The University of Tennessee, May 1993. Unclassified, No Copyright, Unlimited, Publicly available.

[11] D. M. Kipp, J. A. Dec, G. W. Wells, and R. D. Braun. Development of a planetary entry system synthesis tool for conceptual design and analysis. In *Proceedings of the 3rd International Planetary Probe Workshop*, Athens, Greece, June 2005.

[12] I. A. Klepikov, B. I. Katorgin, and V. K. Chvanov. The new generation of rocket engines, operating by ecologically safe propellant "liquid oxygen and liquefied natural gas (methane)". *Acta Astronautica*, 41(4):209–217, 1997.

[13] T. W. Knacke. *Parachute Recovery Systems Design Manual*. Para Pub, 1992.

[14] B. Laub. Ablative thermal protection: An overview. In *55th Pacific Coast Regional and Basic Science Division Fall Meeting*, October 2003. Unclassified, No Copyright, Unlimited.

[15] L. Lees. Laminar heat transfer over blunt-nosed bodies at hypersonic flight speeds. *Jet Propulsion*, pages 259–269, 1956.

[16] F. S. Milos, Y.-K. Chen, W. M. Congdon, and J. M. Thornton. Mars pathfinder entry temperature data, aerothermal heating, and heatshield material response. *Journal of Spacecraft and Rockets*, 36(3):380–391, May-June 1999.

[17] R. A. Minzner, C. A. Reber, L. G. Jacchia, F. T. Huang, A. E. Cole, A. J. Kantor, T. J. Keneshea, S. P. Zimmerman, and J. M. Forbes. Defining constants, equations, and abbreviated tables of the 1975 u.s. standard atmosphere. Technical Report TR R-459, NASA, May 1976.

[18] V. I. Moroz. The atmosphere of venus. *Space Science Reviews*, 29(1):3–127, March 1981.

[19] W. A. Page and H. T. Woodward. Radiative and convective heating during venus entry. *AIAA Journal*, 10:1379–1381, 1972.

[20] D. S. F. Portree. Mir hardware heritage. Technical report, Johnson Space Center, March 1995. NASA RP-1357.

[21] D. J. Rasky and H. K. Tran. Low-cost entry systems for future planetary exploration missions. *Acta Astronautica*, 45(4):347–355, August 1999.

[22] F. J. Regan and S. M. Anandakrishnan. *Dynamics of Atmospheric Re-entry*. AIAA, 1993.

[23] W. I. Scallion and J. H. Lewis. Body motions and angles of attack during project fire flight ii reentry. Nasa technical note, Langley Research Center, October 1967. NASA TN D-4183.

[24] A. Seiff. Post-viking models for the structure of the summer atmosphere of mars. *Advances in Space Research*, 2(2):3–17, 1982.

[25] B. A. Steinfeldt, M. J. Grant, D. M. Matz, R. D. Braun, and G. H. Barton. Guidance, navigation, and control technology system trades for mars pinpoint landing. In *AIAA Atmospheric Flight Mechanics Conference*, Honolulu, HI, August 2008. AIAA 2008-6216.

[26] K. Sutton and R. A. Graves. A general stagnation point convective-heating equation for arbitrary gas mixtures. Technical report, NASA, November 1971. TR R-376.

[27] M. E. Tauber and K. Sutton. Stagnation-point radiative heating relations for earth and mars entries. *Journal of Spacecraft and Rockets*, 28(1):40–42, Jan-Feb 1991.

[28] H. K. Tran, C. E. Johnson, D. J. Rasky, F. C. L. Hui, M.-T. Hsu, T. Chen, Y. K. Chen, D. Paragas, and L. Kobayashi. Phenolic impregnated carbon ablators (pica) as thermal protection systems for discovery missions. Technical Report NASA TM-110440, NASA, April 1997. Unclassified, No Copyright, Unlimited, Publicly available.

[29] S. D. Williams and D. M. Curry. Thermal protection materials - thermophysical property data. Technical report, NASA, December 1992. NASA RP-1289, Unclassified - Unlimited.

[30] T. Yamada, Y. Inatani, N. Ishii, J. Kawaguchi, and T. Abe. Japanese entry/reentry capsules: Past, present, and future. In *6th International Planetary Probe Workshop*, Atlanta, GA, June 2008.

Table 6. Conversion Factors

SI	Imperial
1 kg/m3	6.242782×10^{-2} lbm/ft3
1 kJ/kg-K	2.388459×10^{-1} Btu/lbm-R
1 W/m-k	1.604969×10^{-4} Btu/ft-s-R
1 kJ/kg	4.299208×10^{-1} Btu/lbm

BIOGRAPHY

Richard E Otero is an Aerospace Engineering Ph.D. candidate at the Georgia Institute of Technology. He received a M.S. in Aerospace Engineering in 2009 from Georgia Tech. He received his B.S. in Computer Science from SUNY New Paltz. His work has included the design and development of the Planetary Entry Systems Synthesis Tool (PESST) currently in use at JPL for the conceptual design of entry vehicles. His interests include: multidisciplinary design optimization, global trajectory optimization, automatic problem decomposition and artificial intelligence. He is an Alfred P. Sloan Foundation Ph.D. Scholar and a GEM fellow.

Robert D. Braun is an Associate Professor in the Daniel Guggenheim School of Aerospace Engineering at the Georgia Institute of Technology. As Director of Georgia Tech's Space Systems Design Laboratory, he leads a research program focused on the design of advanced flight systems and technologies for planetary exploration. He is responsible for undergraduate and graduate level instruction in the areas of space eysems design, astrodynamics and planetary entry. Prior to coming to Georgia Tech, Dr. Braun worked at NASA Langley Research Center for sixteen years where he contributed to the design, development, test, and operation of several robotic space flight systems. Dr. Braun is an AIAA Fellow and the principle author or co-author of over 175 technical publications in the fields of planetary exploration, atmospheric entry, multidisciplinary design optimization, and systems engineering.

APPENDIX: THERMAL MATERIAL PROPERTIES

Table 7. PICA Density and Reaction Information. [28]

Component	**Initial Density** (kg/m^3)	**Residual Density** (kg/m^3)	**Pre-exponential Factor** (s^{-1})	**Density Exponent**	**Activation Energy** (K)	**Min Reaction Temp** (K)
Resin (Comp A)	228.26	0.00	1.40000E+04	3.0	8555.56	555.56
Resin (Comp B)	973.12	792.92	4.48000E+09	3.0	20444.45	333.33
Fiber Reinforcement	160.18	160.18	0.00000E+00	0.0	0.00	50000.00

Table 8. PICA Heats of Formation and Resin Fraction. [28]

Resin Volume Fraction	**Virgin Heat of Formation** (kJ/kg)	**Char Heat of Formation** (kJ/kg)	**Pyrolysis Gas Heat of Formation** (kJ/kg)	**Datum Temp for Zero Enthalpy** (K)
0.0646	-875.7	0.0	0.0	297.8

Table 12. FM 5055 Density and Reaction Information. [10]

Component	**Initial Density** (kg/m^3)	**Residual Density** (kg/m^3)	**Pre-exponential Factor** (s^{-1})	**Density Exponent**	**Activation Energy** (K)	**Min Reaction Temp** (K)
Resin (Comp A)	247.97	0.00	2.17100E+01	1.92	4627.22	297.78
Resin (Comp B)	0.00	0.00	1.00000E+00	1.00	0.56	5500.00
Fiber Reinforcement	2231.06	1905.88	9.53500E+10	3.10	19333.33	560.56

Table 13. FM 5055 Heats of Formation and Resin Fraction. [10]

Resin Volume Fraction	**Virgin Heat of Formation** (kJ/kg)	**Char Heat of Formation** (kJ/kg)	**Pyrolysis Gas Heat of Formation** (kJ/kg)	**Datum Temp for Zero Enthalpy** (K)
0.4010	-911.1	0.0	0.0	297.8

Table 9. PICA Virgin Properties for Insulation. [28]

Temp (K)	**Cp** (kJ/kgK)	**k** (W/mK)	ϵ	α
222.2	1.44863	5.48584E-01	0.80	0.80
527.8	1.93430	5.85968E-01	0.80	0.80
833.4	2.34042	6.25887E-01	0.80	0.80
1650.6	2.46603	1.08696E+00	0.80	0.80
2467.8	2.46603	1.54366E+00	0.80	0.80
2608.2	2.46603	1.56327E+00	0.80	0.80
2748.6	2.46603	1.60968E+00	0.80	0.80
2888.9	2.46603	1.64362E+00	0.80	0.80
3333.3	2.46603	1.68100E+00	0.80	0.80

Table 10. PICA Char Properties for Insulation. [28]

Temp (K)	**Cp** (kJ/kgK)	**k** (W/mK)	ϵ	α
294.4	2.93076	9.78212E-01	0.90	0.90
425.0	3.76812	9.90673E-01	0.90	0.90
555.6	4.60548	1.00313E+00	0.90	0.90
833.3	4.60548	1.17136E+00	0.90	0.90
1666.7	4.60548	1.33959E+00	0.90	0.90
3333.3	4.60548	1.71343E+00	0.90	0.90

Table 11. PICA Pyrolysis Gas Entropy. [28]

Temp (K)	**Enthalpy** (kJ/kg)
400	-9.0172E+03
800	-6.1716E+03
1200	-2.2682E+02
1600	1.2874E+03
2000	2.8954E+03
2400	5.2126E+03
2800	9.7202E+03
3200	1.9148E+04
3600	3.3278E+04
4000	4.4557E+04
4400	5.0000E+04
4800	5.3161E+04

Table 14. FM 5055 Virgin Properties for Insulation. [10]

Temp (K)	**Cp** (kJ/kgK)	**k (Across Ply)** (W/mK)	ϵ **(est)**	α **(est)**
311.1	0.96296		0.85	0.85
338.9		8.09984E-01	0.85	0.85
366.7	1.19324		0.85	0.85
422.2	1.29791	9.22136E-01	0.85	0.85
477.8	1.37327	9.78212E-01	0.85	0.85
533.3	1.44445	1.02183E+00	0.85	0.85
588.9	1.48631	1.04052E+00	0.85	0.85
644.4		1.00937E+00	0.85	0.85

Table 15. FM 5055 Char Properties for Insulation. [10]

Temp (K)	**Cp** (kJ/kgK)	**k (Across Ply)** (W/mK)	ϵ **(est)**	α **(est)**
311.1	0.85829		0.85	0.85
366.7	1.00483	9.53289E-01	0.85	0.85
422.2	1.13881		0.85	0.85
477.8	1.23511	1.17136E+00	0.85	0.85
533.3	1.33978		0.85	0.85
588.9	1.44445	1.35828E+00	0.85	0.85
644.4	1.50725		0.85	0.85
700.0	1.57005	1.51405E+00	0.85	0.85
755.6	1.62448		0.85	0.85
811.1	1.67472	1.64489E+00	0.85	0.85
866.7	1.71659		0.85	0.85
922.2	1.75846	1.67604E+00	0.85	0.85
977.8	1.77520		0.85	0.85
1033.3	1.79614		0.85	0.85
1088.9	1.80870	1.67604E+00	0.85	0.85

Table 16. FM 5055 Pyrolysis Gas Entropy. [10]

Temp (K)	**Enthalpy** (kJ/kg)
294.44	-3661.6
555.56	-2734.0
833.33	-1547.0
1111.1	-153.5
1200.0	351.2
1388.9	1093.2
1666.7	2046.9
1944.4	2930.8
2250.0	3981.4
2500.0	5036.0
2750.0	6298.1
3000.0	7944.0
3250.0	10186.1
3500.0	13254.8
3750.0	17358.5
4055.6	22602.8